POLITECNICO DI TORINO
Repository ISTITUZIONALE

Enhanced 3D Electrochemical-Electromagnetic Model of Cylindrical Li-Ion Batteries for Higher Fidelity Modelling of High-Frequency Impedance Spectra

Original
Enhanced 3D Electrochemical-Electromagnetic Model of Cylindrical Li-Ion Batteries for Higher Fidelity Modelling of High-Frequency Impedance Spectra / Di Prima, P., Mele, I., Bodoardo, S., Santarelli, M., Katrašnik, T., Amici, J.. - In: JOURNAL OF THE ELECTROCHEMICAL SOCIETY. - ISSN 1945-7111. - 173:(2026). [10.1149/1945-7111/ae94f5]

Availability:
This version is available at: 11583/3016014 since: 2026-09-28T11:25:55Z

Publisher:
Institute of Physics - IOP

Published
DOI:10.1149/1945-7111/ae94f5

Terms of use:

This article is made available under terms and conditions as specified in the corresponding bibliographic description in the repository

Publisher copyright

(Article begins on next page)

11 November 2026

Journal of The
Electrochemical Society

OPEN ACCESS

Enhanced 3D Electrochemical-Electromagnetic Model of Cylindrical Li-Ion Batteries for Higher Fidelity Modelling of High-Frequency Impedance Spectra

To cite this article: Piera Di Prima *et al* 2026 *J. Electrochem. Soc.* **173** 160502

View the article online for updates and enhancements.

You may also like

- Electrochemical-Electromagnetic Coupled Physics-Based Mathematical Modeling of Li-Ion Batteries: A Theoretical Proof of Concept
Paul T. Coman, Rafid Mollah, Nicholas Irish et al.
- An Exact Closed-Form Impedance Model for Porous-Electrode Lithium-Ion Cells
Xiangdong Kong, Gregory L. Plett, M. Scott Trimboli et al.
- Three-Electrode Setups for Lithium-Ion Batteries
M. Ender, J. Illig and E. Ivers-Tiffée

The New PAT-Cell-Solid!

EL-CELL® electrochemical test equipment

Cycle Solid-State Batteries Under Controlled Pressure of up to 300 MPa (6 mm Diameter)!

- Adjust and measure a force of up to 9000 N on the cell stack!
  Force adjustment possible throughout the entire experiment
- Built-in force, and temperature sensors!
  With optional gas pressure sensor and gas in- and outlet
- PAT-Solid-Core for easy assembly and reproducible results!
  Press and cycle solid-state batteries with 6 or 10 mm electrode diameter
- Cableless and highly sealed battery test cell!
  For precise long-term measurements of solid-state cell chemistries

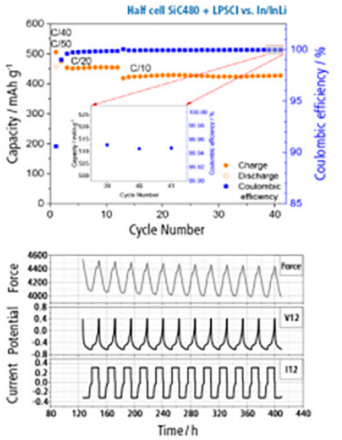

Learn more on our product website: Scan me!

Download the data sheet (PDF): Scan me!

Or contact us directly:
+49 40 79012-734
sales@el-cell.com
www.el-cell.com

This content was downloaded from IP address 130.192.232.210 on 24/08/2026 at 09:50

Journal of The Electrochemical Society, 2026 **173** 160502

Enhanced 3D Electrochemical-Electromagnetic Model of Cylindrical Li-Ion Batteries for Higher Fidelity Modelling of High-Frequency Impedance Spectra

Piera Di Prima,[1,2] Igor Mele,[3] Silvia Bodoardo,[1] Massimo Santarelli,[4] Tomaž Katrašnik,[3,z] and Julia Amici[1]

[1]*Department of Applied Science and Technology, Politecnico di Torino, Corso Duca degli Abruzzi 24, Torino 10129, Italy*
[2]*Reefilla srl, Lungo Dora P. Colletta 85, Torino 10153, Italy*
[3]*University of Ljubljana, Faculty of Mechanical Engineering, Ljubljana SI-1000, Slovenia*
[4]*Department of Energy, Politecnico di Torino, Corso Duca degli Abruzzi 24, Torino 10129, Italy*

This study presents a modelling framework for fully coupled modelling of electrochemical-electromagnetic phenomena in 3D with a focus on higher frequency intra-cell phenomena. The model integrates a porous electrode theory based electrochemical model with the Maxwell–Ampère law model and innovatively considers the full 3D geometry of the cell with an aim to more accurately represent its internal structure. It is shown in the paper that full coupling of electrochemical and electromagnetic phenomena on the same 3D computational mesh makes possible higher fidelity simulations of high-frequency inductive effects in realistic cell geometries. The properties and capabilities of the model are demonstrated on the cylindrical 21 700 Li-ion cell. The results clearly show that the 3D geometry of the jellyroll structure of the cylindrical cell with its spiral arrangement of electrodes and current collectors significantly influences the distribution of currents and thus the inductive response at high frequencies. These improved predictive capabilities of the model, especially in the description of high-frequency impedance phenomena, enable a deeper understanding of how design features influence the electrochemical impedance spectroscopy (EIS) response of the battery and open new perspectives for the model-based deciphering of EIS spectra of cells with pronounced high-frequency inductive effects.

© 2026 The Author(s). Published on behalf of The Electrochemical Society by IOP Publishing Limited. This is an open access article distributed under the terms of the Creative Commons Attribution 4.0 License (CC BY, https://creativecommons.org/licenses/by/4.0/), which permits unrestricted reuse of the work in any medium, provided the original work is properly cited.
[DOI: 10.1149/1945-7111/ae94f5]

Manuscript submitted April 3, 2026; revised manuscript received July 17, 2026. Published August 14, 2026.

Lithium-ion (Li-ion) batteries have become essential for efficient and reliable energy storage, powering devices ranging from portable electronics to electric vehicles. However, optimizing their performance and lifespan requires a deeper understanding of their internal electrochemical processes. In this context, electrochemical impedance spectroscopy (EIS) offers valuable insights into the complex dynamics of Li-ion batteries.

Electrochemical impedance spectroscopy is one of the most important techniques for the non-invasive characterization of batteries.[1–3] The standard measurement method uses a sinusoidal voltage or current with a specific amplitude and frequency and measures the response of the device in terms of the resulting voltage or current amplitude and phase shift. This procedure is usually repeated in a frequency range from kHz to mHz, generating an impedance spectrum that analyzes processes with different time constants within the battery. When evaluating the results, Nyquist and Bode plots are usually used to facilitate the parameterisation of the resistance, capacitance and inductance associated with different electrochemical processes. However, the impedance response of commercial Li-ion batteries includes contributions from various internal components, and different electrochemical processes have similar time constants, making it challenging to analyze the results.[1]

Looking at the Nyquist plot, the inductive behavior in the high frequency range of the spectrum could be attributed to the cell geometry, especially in batteries with a jellyroll configuration, or it could be an artefact caused by the wire connections.[4–6] In general, the first intersection with the real axis represents the sum of the ohmic resistances of the electrolyte, the active materials, the current collector and the electrical contacts.[7,8] However, as also shown in this paper, this intersection point is influenced by high-frequency inductive phenomena in cells in which these phenomena are pronounced. In the medium frequency range, the electrochemical processes at the electrode-electrolyte interfaces exhibit both capacitive and resistive effects and form arcs.[7,9] Finally, the low-frequency tail is an indication of lithium-ion diffusion in the active electrode material.[1,10]

Mathematical models have been developed to better analyze the impedance results. Meyers et al. introduced a single particle model to study the electrochemical impedance response of an intercalation particle that takes into account diffusion, charge transfer processes and the double layer effect.[11,12] Sikha and White[13] presented an analytical model to simulate the impedance response of a cell with an insertion electrode and a metal foil anode, taking into account lithium intercalation kinetics, charge and mass balances in both the solid and electrolyte phases, and adsorption in the double layer.

In addition to these single-particle models, there are physics-based continuum models based on the work of Newman and colleagues.[14–17] These models are based on the pseudo-2-dimensional (P2D) approach, where the battery geometry is simplified into a 1D domain representing the thickness of elements such as porous electrodes and separators, which is then coupled with another domain representing the radius of the active material particles. Wimarshana et al.[18] developed a multi-step parameter identification framework that utilises EIS simulation to improve the accuracy of physics-based models. Kong et al.[19] demonstrated a modified P2D model to simulate and diagnose internal short circuits, emphasising the use of EIS to detect impedance changes. Laue et al.[20] presented the parameter identifiability of electrochemical P2D models and emphasised the importance of simulating both EIS and galvanostatic measurements to ensure accurate model parameterisation. Xie et al.[21] developed and validated a multiphysics EIS simulation approach for lithium-ion batteries. The model considers the growth of the SEI film, charge transport, mass transfer and thermal effects to simulate the impedance changes of the battery during cycling.

Despite these advances, there are still specific challenges when higher fidelity modelling and model-based deciphering of EIS spectra is considered. Recently, a high-fidelity time-domain electrochemical model has been developed that can consistently replicate experimental EIS spectra with three superimposed high-frequency

[z] E-mail: tomaz.katrasnik@fs.uni-lj.si

semicircles, a transition to a diffusion tail at elevated complex values, and a tilted diffusion tail at low frequencies.[22] This model enables higher fidelity modelling and model-based deciphering of the measured EIS spectra, whereas it does not take into account the inductive effects at high frequencies,[23] which are still a challenge. Laman et al.[6] conducted one of the first studies that investigated the physical nature of inductive contributions and emphasised the importance of the spiral-wound geometry of current collectors in influencing the inductive properties of cylindrical cells. Coman et al.[5] developed a new physics-based model for predicting high-frequency impedance in commercial cells with a jellyroll configuration to overcome the limitations of the P2D model.[5] This model integrates electrochemical and electromagnetic equations to investigate the behavior of cylindrical lithium-ion batteries under AC perturbations. The approach combines the electrochemical dynamics of the P2D model, which is based on the porous electrode theory, with an electromagnetic model that treats the jellyroll in a simplified way as a homogeneous cylindrical region with effective material properties instead of explicitly modelling each spirally wound layer. The geometric simplification considers a central mandrel surrounded by the homogenised cylindrical region representing the jellyroll. This method has specific limitations, especially when coupled with the P2D model to simulate the electrochemical behavior of the cell, since the simplified geometry of the electromagnetic model affects the accuracy of the simulations of the potential field and current density, which limits the accuracy of the electrochemical model and thus limits the accurate simulation of the current and lithium ion concentration distributions in the jellyroll configuration in coupled electrochemical, transport and electromagnetic phenomena. Consequently, these geometric simplifications in the electromagnetic model lead to discrepancies between the observed and simulated inductive behavior of the realistic cell.

This study presents a generic modelling framework for the fully coupled modelling of electrochemical-electromagnetic phenomena in 3D, with a focus on higher frequency phenomena. The features and capabilities of the model are demonstrated using the cylindrical 21 700 Li-ion cell, which represents a realistic yet descriptive geometry to demonstrate the importance of a consistent 3D geometric representation of the cell. Indeed, the proposed model enables a more realistic representation of the impedance characteristics over a wide frequency range by combining the electrochemical model with the Maxwell–Ampère law on a realistic 3D geometry. This approach enables a spatially resolved simulation of the current paths, allowing a better understanding of the inductive contributions in the high-frequency impedance responses by explicitly incorporating the complex geometry of the jelly roll and also taking into account the placement of the tabs. The ability to accurately simulate inductive behavior makes this model a valuable tool for battery engineers looking to optimize cell design, minimize parasitic effects and improve overall efficiency, as well as for model-based deciphering of the EIS spectra of cells with pronounced high-frequency inductive effects.

Electrochemical impedance spectroscopy traditionally focuses on the mid-to-low frequency regions[24] where charge transfer and mass transport phenomena govern the system behavior. The high-frequency inductive tail has historically been dismissed as an experimental artifact or a consequence of external cable arrangements. Modern battery research has radically redefined this perspective, demonstrating that the high-frequency response encapsulates a wealth of information regarding the internal structural integrity and physical architecture of the cell. Rapid signal acquisition in the millisecond range makes this specific spectral zone highly valuable for detecting structural anomalies, current collector degradation, and localized mechanical shifts within the jellyroll.[25,26] Decoupling these complex, spatially heterogeneous phenomena demands a modelling framework capable of bridging microscopic electrochemical kinetics with macroscopic electromagnetic field distributions.

Standard impedance models often simplify the governing equations by assuming that a small input signal spreads out uniformly across the entire cell.[24,27] However, this assumption fails at high frequencies because the current concentrates heavily around the current collector tabs, causing severe localized current crowding.[28,29] Even when the total applied current perturbation is low, these local spikes push the electrochemical reactions far outside the conventional linear range, making the full non-linear Butler–Volmer kinetics necessary to capture the real physical gradients.[27,30] Accounting for these non-linear local distributions is vital because they serve as the direct spatial source terms linking the electrochemical domain to the macroscopic electromagnetic fields.

Pseudo-four-dimensional (P4D, i.e. 3D cell geometry and 1D active particle resolution) multiphysics models provide this exact capability, offering the spatial resolution necessary to capture current crowding and inductive variations. These advanced digital twins establish the foundational physical correlations required to train data-driven diagnostic tools, parameterise equivalent circuits, and optimize cell design before physical prototyping.

Model Description

In this study, a comprehensive model for simulating the impedance behavior of cylindrical batteries is developed by integrating a physics-based electrochemical model with an electromagnetic model that can capture inductive effects. The model has been developed for impedance spectroscopy, in particular to analyze the complex interplay between electrochemical phenomena and the inductive behavior of the jellyroll configuration of the cell under alternating potential perturbations, taking into account realistic 3D geometries of cells. Previous models, such as the widely used P2D model, have proven successful in capturing electrochemical processes but were unable to accurately predict the high-frequency impedance response due to their inherent one-dimensional geometry. These limitations restrict the ability to resolve spatial variations in the current paths and thus the inductive effects caused by the jellyroll structure. In contrast, the P4D model proposed in this work improves the battery spatial resolution by incorporating its full three-dimensional geometry, resulting in a more accurate representation of its internal structure while also considering the position of the tabs that influence the current path in the jellyroll. This approach not only improves simulation accuracy, but also provides a better understanding of how design features can affect battery performance. This localized feedback mechanism demonstrates that high-frequency impedance features are not merely a bulk material property but are strongly dictated by the internal geometric pathways and architectural constraints of the commercial cylindrical configuration.

Electrochemical and transport model equations.—The electrochemical and transport part of the model is based on porous-electrode theory, which is applied to the 3D geometry to represent the real structure of the electrodes. The governing equations are based on the conservation principles for mass and charge.

Considering the frequency domain, for the electrolyte, the conservation of mass is described by the equation:

$$\epsilon_l \mathrm{i}\omega c_l = \nabla \cdot \left(D_l^{\mathrm{eff}} \nabla c_l\right) + \frac{a\left(j_{\mathrm{loc,f}} + j_{\mathrm{loc,cdl}}\right)}{F}\left(1 - t_+\right) \qquad [1]$$

where ω is the angular frequency, c_l is the concentration of lithium ions in the electrolyte, ϵ_l is the electrolyte volume fraction, and D_l^{eff} is the effective diffusion coefficient, corrected for tortuosity using the Bruggeman correlation. The terms $j_{\mathrm{loc,f}}$ and $j_{\mathrm{loc,cdl}}$ represent the local current densities associated with faradaic processes and double-layer capacitance, respectively, where a is the electrolyte-electrode specific surface area, and F is Faraday's constant. The effective

diffusion coefficient, $D_{\mathrm{l}}^{\mathrm{eff}}$, is corrected as:

$$D_{\mathrm{l}}^{\mathrm{eff}} = D_{\mathrm{l}}\epsilon_{\mathrm{l}}^{1.5}. \quad [2]$$

The conservation of charge in the liquid electrolyte is expressed as:

$$\nabla\cdot\left(-\sigma_{\mathrm{l}}^{\mathrm{eff}}\nabla\phi_{\mathrm{l}}\right)+\nabla\cdot\left(\frac{2RT\sigma_{\mathrm{l}}^{\mathrm{eff}}}{F}\left(1+\frac{\partial\ln\left(f\right)}{\partial\ln\left(c_{l}\right)}\right)\left(1+t^{+}\right)\nabla c_{\mathrm{l}}\right) = a\left(j_{\mathrm{loc,f}}+j_{\mathrm{loc,cdl}}\right), \quad [3]$$

where ϕ_{l} and c_{l} represent the electric potential and lithium-ion concentration in the electrolyte, respectively, f is the activity coefficient, T is the temperature, R the universal gas constant and $\sigma_{\mathrm{l}}^{\mathrm{eff}}$ is the effective ionic conductivity of the electrolyte, which is corrected for the porous nature of the electrode using the Bruggeman correlation to account for tortuosity:

$$\sigma_{\mathrm{l}}^{\mathrm{eff}} = \sigma_{\mathrm{l}}\epsilon_{\mathrm{l}}^{1.5}. \quad [4]$$

Zero-flux boundary conditions are applied at the interface between the current collector and the porous electrode:

$$\nabla c_{l}|_{neg,current\ collector}^{interface} = \nabla c_{l}|_{pos,current\ collector}^{interface} = 0 \quad [5]$$

$$\nabla\phi_{l}|_{neg,current\ collector}^{interface} = \nabla\phi_{l}|_{pos,current\ collector}^{interface} = 0. \quad [6]$$

The equation describing the conservation of lithium ions in the solid phase in the frequency domain is given below:

$$\mathrm{i}\omega c_{\mathrm{s}} = \frac{\partial}{\partial r}\left(\left(-\frac{F}{RT}\left(\frac{c_{\mathrm{s,max}}-c_{\mathrm{s}}}{c_{\mathrm{s,max}}}\right)c_{\mathrm{s}}\frac{\partial E_{\mathrm{eq}}}{\partial c_{\mathrm{s}}}\right)D_{\mathrm{s}}\frac{1}{r^{2}}\frac{\partial}{\partial r}\left(r^{2}\frac{\partial c_{\mathrm{s}}}{\partial r}\right)\right), \quad [7]$$

where c_{s} is the concentration of lithium in the solid phase, D_{s} and E_{eq} are the diffusion coefficient of the solid active material and the equilibrium potential of the electrode both dependent on the lithium concentration inside the particle. Two boundary conditions are applied, the first states that the concentration of intercalated ions does not change at the centre of the particle, meaning no flux occurs there. The second specifies that the ion flux at the particle surface equals the rate of the electrochemical reaction at the interface:

$$-D_{\mathrm{s,i}}\frac{\partial c_{\mathrm{s,i}}}{\partial r}|_{r=0} = 0, \quad [8]$$

$$-D_{\mathrm{s,i}}\frac{\partial c_{\mathrm{s,i}}}{\partial r}|_{r=R_{\mathrm{p,i}}} = \frac{j_{\mathrm{loc,f}}}{F}. \quad [9]$$

Charge conservation in the solid phases is governed by:

$$\nabla\cdot\left(-\sigma_{\mathrm{s}}^{\mathrm{eff}}\nabla\phi_{\mathrm{s}}\right) = a\left(j_{\mathrm{loc,f}}+j_{\mathrm{loc,cdl}}\right). \quad [10]$$

Here, $\sigma_{\mathrm{s}}^{\mathrm{eff}}$ represents the effective electric conductivity of the solid electrode, which is corrected using the Bruggeman relation:

$$\sigma_{\mathrm{s}}^{\mathrm{eff}} = \sigma_{\mathrm{s}}\epsilon_{\mathrm{s}}^{\mathrm{brugg}}. \quad [11]$$

In this equation, ϵ_{s} denotes the volume fraction of the solid phase, σ_{s} is the conductivity of the solid material, and *brugg* is the Bruggeman coefficient derived from the electrode tortuosity and takes values of 1.7 for the anode and 1.94 for the cathode. At the boundary of the positive tab, the applied sinusoidal perturbation of 15 mV ($\tilde{V}_{\mathrm{app}}$) is specified, while a ground boundary condition is applied at the negative tab of the battery:

$$-D\sigma_{\mathrm{eff}},p\left.\frac{\partial\phi_{s,p}}{\partial r}\right|_{\mathrm{positive\ tab}} = \tilde{V}_{\mathrm{app}}, \quad [12]$$

$$-D\sigma_{\mathrm{eff,p}}\left.\frac{\partial\phi_{\mathrm{s,n}}}{\partial r}\right|_{\mathrm{negatove\ tabs}} = 0. \quad [13]$$

The local current density resulting from the double-layer effect at the surface of the electrode particles is expressed as:

$$j_{\mathrm{loc,cdl}} = \mathrm{i}\omega\left(\Phi_{\mathrm{s}}-\Phi_{\mathrm{l}}\right)c_{\mathrm{dl}}. \quad [14]$$

The Butler–Volmer kinetics expression is employed to model the electrochemical reactions in lithium-ion systems. This expression describes the current density $j_{\mathrm{loc,f}}$ as a function of the overpotential η, accounting for both anodic and cathodic processes:

$$j_{\mathrm{loc,f}} = k_{0}Fc_{\mathrm{s,max}}\sqrt{\frac{c_{\mathrm{l}}}{c_{\mathrm{l,ref}}}}\sqrt{\frac{c_{\mathrm{s}}}{c_{\mathrm{s,max}}}\left(1-\frac{c_{\mathrm{s}}}{c_{\mathrm{s,max}}}\right)}\left\{\exp\left[\frac{\alpha_{\mathrm{a}}F\eta}{RT}\right]-\exp\left[\frac{\alpha_{\mathrm{c}}F\eta}{RT}\right]\right\}. \quad [15]$$

In this equation, k_0 represents the reaction rate, while α_{a} and α_{c} are the anodic and cathodic charge transfer coefficients, respectively. The overpotential η in this context is defined as:

$$\eta = \Phi_{\mathrm{e}}-\Phi_{\mathrm{l}}-E_{\mathrm{eq}}. \quad [16]$$

Electromagnetic model equations.—The electromagnetic part of the model is developed to capture the inductive effects, particularly in the jellyroll configuration. The model is governed by Maxwell–Ampère law, describing the relationship between the current density and the magnetic field:

$$\nabla\times\boldsymbol{H} = \boldsymbol{J}_{\mathrm{em}}, \quad [17]$$

where $\boldsymbol{H}$ is the magnetic field vector and $\boldsymbol{J}_{\mathrm{em}}$ is the current density vector. The current density in the frequency domain is expressed as:

$$\boldsymbol{J}_{\mathrm{em}} = \sigma\boldsymbol{E}+\mathrm{i}\omega\boldsymbol{D}, \quad [18]$$

where σ is the electrical conductivity, $\boldsymbol{E}$ is the electric field defined as:

$$\boldsymbol{E} = -\nabla\phi_{\mathrm{s}}-\mathrm{i}\omega\boldsymbol{A}, \quad [19]$$

where $\boldsymbol{A}$ is the magnetic vector potential. The electric displacement field $\boldsymbol{D}$ is defined as:

$$\boldsymbol{D} = \epsilon_{0}\epsilon_{\mathrm{r}}\boldsymbol{E}, \quad [20]$$

where ϵ_0 is the permittivity of free space and ϵ_{r} is the relative permittivity of the materials in the jellyroll. Finally, the magnetic flux density vector is defined as:

$$\boldsymbol{B} = \nabla\times\boldsymbol{A}. \quad [21]$$

Each component of the cell is modelled considering its specific properties. Thus, the separator is treated as an electric insulator. Absorbing boundary condition are applied at the external surfaces.[5] The solid-phase current density vectors obtained from the electrochemical model serve as inputs to the Maxwell–Ampère equations. The term J_{ec} represents the interfacial charge transfer reactions

occurring at the electrode–electrolyte interface, which follow Butler–Volmer kinetics, and also includes double-layer charging effects. Thus, Eq. 18 can be written considering the current density vectors of the electrochemical model:

$$\boldsymbol{J}_{\text{tot}} = \boldsymbol{J}_{\text{em}} + \boldsymbol{J}_{\text{ec}}, \quad [22]$$

and the charge conservation condition is imposed by:

$$\nabla \cdot \boldsymbol{J}_{\text{tot}} = \mathbf{0}. \quad [23]$$

The integration of the electromagnetic domain with the electrochemical framework relies on a fully coupled solver scheme to accurately capture the high-frequency behavior of the cell under alternating current perturbations. This simultaneous solution strategy is essential for representing the complex bidirectional interactions occurring within the wound jellyroll geometry. Within this time-harmonic framework, localized transport phenomena are directly linked to the field equations; specifically, the local current densities arising from both faradaic reactions and double-layer charging processes act as the core source term, $\boldsymbol{J}_{\text{ec}}$, for the Maxwell–Ampère formulation. In this manner, the electrochemical flux distribution serves as the physical driver that generates the internal magnetic fields. Conversely, a mathematical feedback loop is established as the calculated magnetic vector potential feeds back into the charge transport equations. This coupling manifests in the electric field definition through the inductive term $-\mathrm{i}\omega\boldsymbol{A}$, which physically accounts for the induced electromotive force arising from the spiral current loops within the current collector foils. By opposing the local scalar potential gradient, this induced field directly alters the solid-phase potential Φ_{s} distribution. Consequently, it shifts the local activation overpotentials, η, and dictates the overall high-frequency response, ultimately leading to the characteristic phase shifts observed in the impedance spectra.

The inductance generated within the jellyroll of the battery can be defined using Stokes' theorem and the relationship between the magnetic vector potential and the magnetic field. In this structure, current flowing through the conductive layers generates a magnetic field, inducing magnetic flux through the surface enclosed by the current path. The inductance $\mathcal{L}$ is the ratio of the magnetic flux φ linked with the coil to the current producing it, expressed as:

$$\mathcal{L} = \frac{\varphi}{I_{\text{app}}}. \quad [24]$$

The flux φ can be determined by integrating the magnetic field $\boldsymbol{B}$ over a surface S using:

$$\varphi = \int \boldsymbol{B} \cdot \mathbf{n}\, \mathrm{d}A, \quad [25]$$

where $\mathbf{n}$ is the unit normal vector to the surface. Expressing $\boldsymbol{B}$ in terms of the magnetic vector potential, $\boldsymbol{A}$, and applying Stokes' theorem, the surface integral is converted into a line integral around the path enclosing the surface. Thus, the inductance can be described linking the current, the induced magnetic field, and the resulting magnetic flux by:

$$\mathcal{L} = \frac{1}{I_{\text{app}}} \oint \boldsymbol{A} \cdot \boldsymbol{t}\, \mathrm{d}\ell, \quad [26]$$

where $\boldsymbol{t}$ is the tangent vector to the closed curve ℓ.

The total impedance combines the contributions from the electrochemical and electromagnetic models, with the electrochemical model dominating at low frequencies and the electromagnetic model contributing at higher frequencies where inductive effects become more pronounced. The impedance from the electrochemical model is calculated at the boundary of the positive electrode tab. The total impedance, Z, is then evaluated by:

$$Z = \mathrm{i}\omega\mathcal{L} + \frac{\Phi_{\text{s}}}{\boldsymbol{I}_{\boldsymbol{s,n}}}, \quad [27]$$

where $\boldsymbol{I}_{\boldsymbol{s,n}}$ is the current vector normal to the boundary of the positive tab.

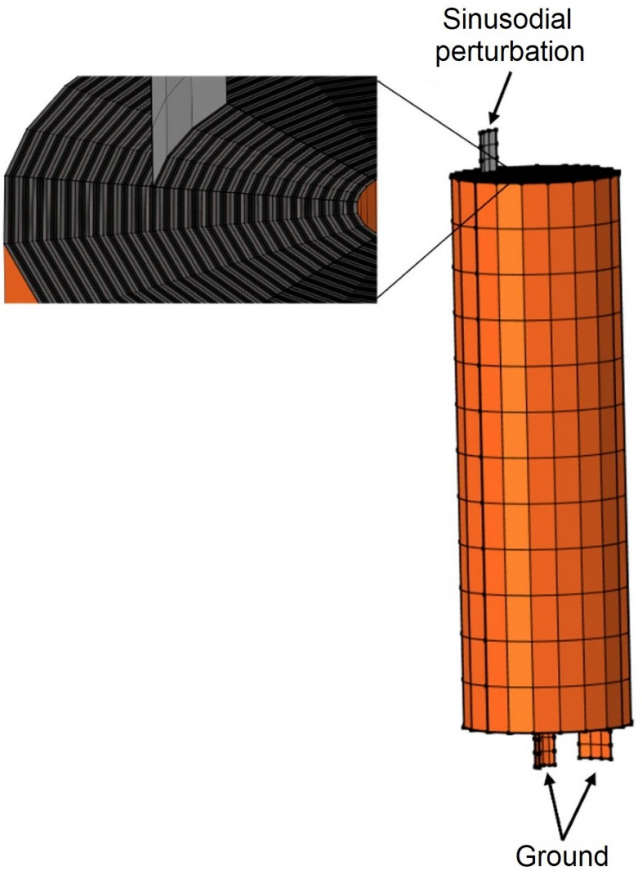

Figure 1. 3D geometry used in the simulation, with a magnified section of the mesh showing the internal layers of the cylindrical cell.

Geometry, mesh and solution method.—The 3D shape of the cell in this study is adapted from the internal design of the LGM50LT cell. The geometry of the jellyroll structure was calculated using the Archimedean spiral equation with 24.5 windings. The cell contains two anode tabs: one inner tab located near the core of the jellyroll and one outer tab positioned at the outer end of the anode current collector, as well as a single cathode tab at the centre of the cathode current collector. Baazouzi et al.'s work[31] provides additional information on the structural layout. Figure 1 shows the 3D geometry used in the simulation, including a magnified section of the mesh that highlights the internal layers of the cylindrical cell.

In order to develop an accurate and reliable P4D model, the selection of quadrilateral (quad) meshes and the application of geometry partitioning were essential. Quadrilateral meshes improve computational efficiency by reducing the number of singular points and producing a more accurate representation of geometric models with fewer elements.[32] In order to generate a quad mesh, regions containing the tabs underwent to geometry partitioning. This quad mesh and geometry partitioning combination improved convergence while

Table I. Model parameters.

Parameters	Negative electrode	Positive electrode	Separator
Thickness, L (m)	85.2×10^{-6}	58.3×10^{-6}	12×10^{-6}
Current collector thickness, L (m)	12×10^{-6}	16×10^{-6}	
Mean particle radius, R_p (m)	5.05×10^{-6}	5.22×10^{-6}	
Active material volume fraction, ε_s (−)	0.728	0.706	
Electrolyte volume fraction, ε_l (−)	0.272	0.294	0.47
Bruggeman exponent, b (−)	1.7	1.94	1.5
Maximum lithium concentration, $c_{s,\,max}$ (mol m^{-3})	28 590	51 545	
Reaction rate, k_0 (m s^{-1})	1×10^{-9}[b]	7×10^{-9}[b]	
Diffusion coefficient, D_s (m^2 s^{-1})	Figure. 3b	Figure. 3a	
Equilibrium potential, E_{eq} (V)	Figure. 2b	Figure. 2a	
Double layer capacitance (F m^{-2})	0.05[b]	3.5[b]	
Electric conductivity (S m^{-1})	215[34]	0.84[34]	1×10^{-16}[35]
Current collector electric conductivity (S m^{-1})	5.998×10^{7}[a]	3.774×10^{7}[a]	
Relative permittivity, ε_r (−)	20[36,37]	18.5[38]	20[36,37]
Film resistance (Ω m^2)	0.026[39]	8.5×10^{-3}[40]	
Physical constant			
Ideal gas constant, R (J (K·mol)$^{-1}$)	8.314		
Faraday constant, F (s·A mol^{-1})	96 485		

a) COMSOL Multiphysics® Material Library.
b) Fitted.

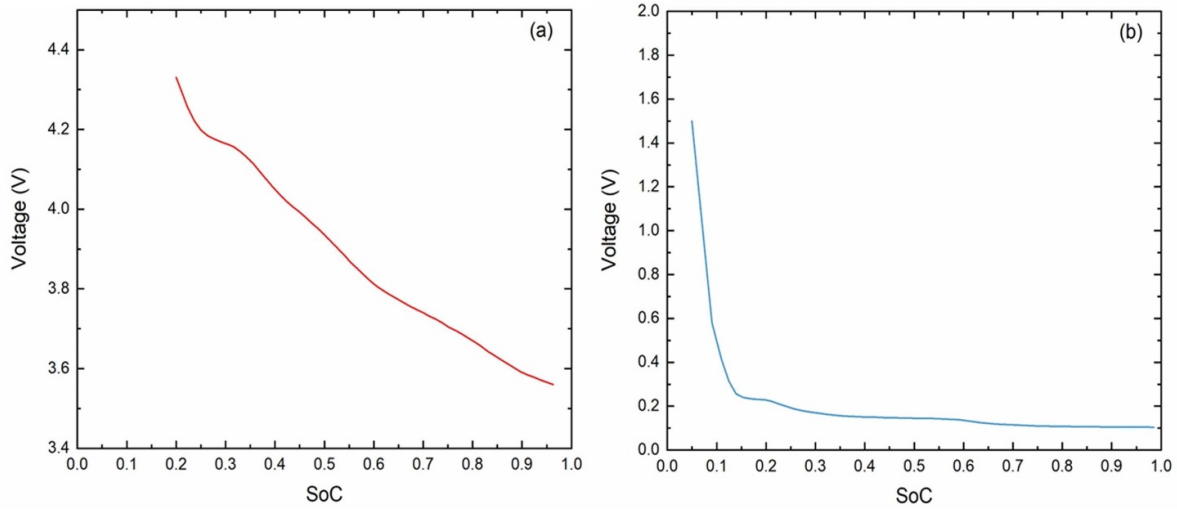

Figure 2. Equilibrium potential of cathode (a) and anode (b).

reducing the overall amount of mesh components. With 155 996 quad elements in the finished mesh, accuracy and computational efficiency are optimally balanced. COMSOL Multiphysics offers a range of solvers to address various physics-based problems. The choice of solver depends on the complexity of the problem, the required accuracy, and available computational resources. The coupled electrochemical-electromagnetic model was solved using COMSOL Multiphysics with a fully coupled approach and the direct solver algorithm (MUMPS). In order to guarantee numerical stability and convergence, Newton's iterative approach was used with a damping factor of 1. Table I reports the model parameters, while the equilibrium curves and diffusion coefficients of both electrodes are shown in Figs. 2 and 3, respectively. All parameters were experimentally determined, except for those denoted by an uppercase letter or sourced from articles listed in the references. The experimental procedures, instruments, and parameter extraction methods for these specific cells are described in our previous work.[33]

Experimental

The aim of this study was to investigate the inductive effects in cylindrical cells, focusing on the high-frequency behavior. Potentiostatic impedance spectroscopy measurements were performed on a LGM50LT cell charged to 50%, with a frequency range from 0.1 Hz to 5 kHz and an oscillating voltage with an amplitude of 15 mV. The measurements were performed with a resolution of 10 points per decade at room temperature. As the low-frequency diffusion tail was outside the scope of this study, it was not investigated. Impedance responses were recorded using a VMP-3 Biologic multichannel potentiostat. The experimental characterization was

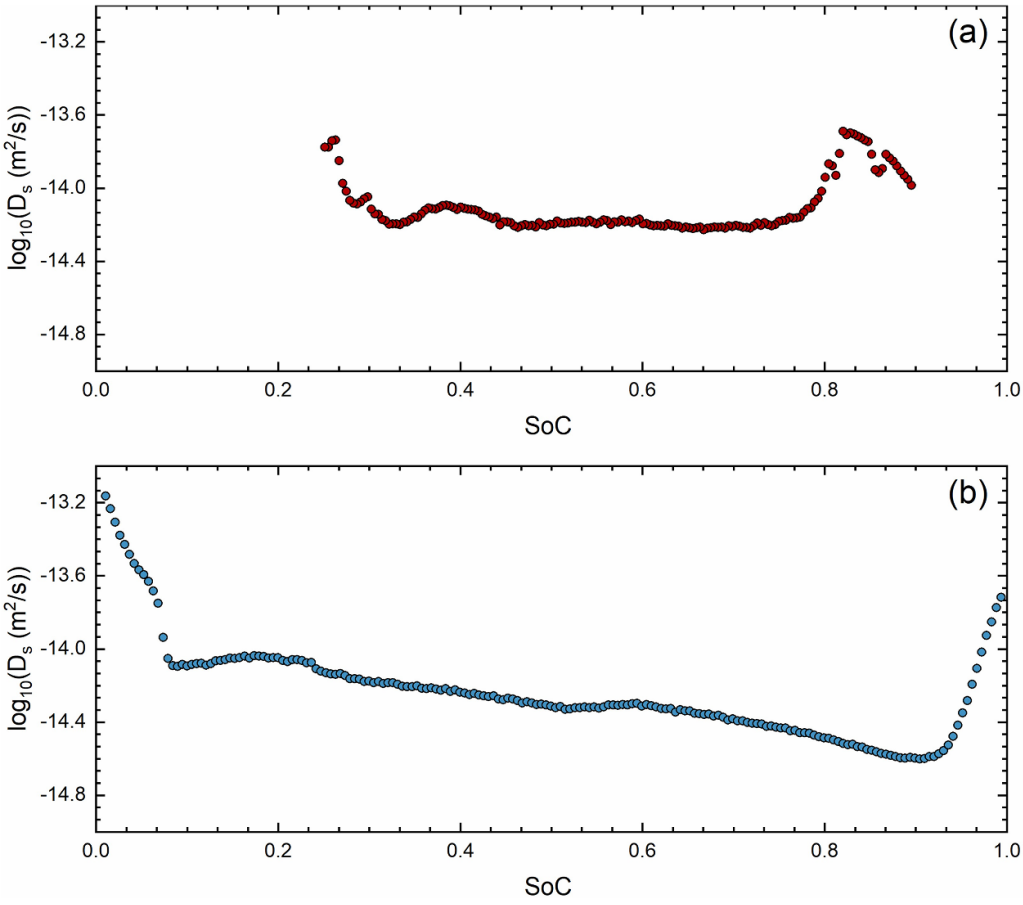

Figure 3. Diffusion coefficient of cathode (a) and anode (b).

conducted on three identical cells to ensure reproducibility. Each cell was positioned in a specialised low-contact-resistance holder coupled with a four-wire connection to minimize connection impedance. Within the analyzed frequency window (up to 5 kHz), the inductive behavior is dictated by the internal spiral geometry of the jellyroll and the specific tab layout. While inductive responses at higher frequencies can often be an artifact caused by the wire connections, such external parasitic lead effects are typically prominent only at frequencies significantly higher than 5 kHz.[25] Consequently, the high-frequency impedance features observed reflect the physical configuration of the cell rather than cable arrangement artefacts.

Results and Discussion

The electrochemical equations for mass conservation, charge conservation and Butler–Volmer kinetics provide information on charge transport and reaction kinetics, which primarily influence the impedance in the low frequency range. In the Maxwell–Ampère equation, inductive effects in the high-frequency range are explicitly taken into account, which emphasises the role of the jellyroll configuration in shaping the impedance characteristics.

The electrochemical P4D model, which was analyzed in the frequency domain considering the double layer capacitance, effectively describes the main aspects of the AC response. However, since it does not take into account the interactions with the magnetic field, the model fails to replicate the inductive effects that appear in the experimental data, as shown in Fig. 4. This limitation is due to the lack of electromagnetic coupling, which becomes increasingly important at higher frequencies. Coupling the P4D model with the electromagnetic model improves the simulation results at high frequencies, as shown in the Nyquist plot in Fig. 4a.

In the electrochemical model, the current densities are determined by the potential gradients and are responsible for driving the electrochemical reactions in the battery. These current densities act as sources of the magnetic field (Eq. 21), linking the current flow with the generated magnetic field. The geometry of the jellyroll configuration with its spiral arrangement of electrodes and current collectors plays an important role in the distribution of these currents and the resulting magnetic field. The magnetic field together with the associated current vector at 0.1 kHz–5 kHz are shown in Fig. 5, which illustrates the importance of accurately representing the full 3D cell geometry when analyzing high-frequency phenomena in cells with pronounced high-frequency inductive effects.

At higher frequencies, the magnetic field induces inductive effects that influence the impedance of the battery. However, as the 1D approximation of the P2D model does not fully capture the complex current distribution and magnetic field interactions in this intricate geometry, the applied P4D model provides a higher fidelity representation of the electrochemical and electromagnetic coupling, capturing the detailed current flow, magnetic field generation and resulting inductive contributions, thus improving the prediction of battery behavior, especially in the presence of AC perturbations.

The behavior of the phase angle shown in Fig. 4b is further evidence of the presence of inductive effects. This behavior indicates that as the frequency increases, the interaction between electric current and magnetic fields contributes more to the response of the system, which clearly highlights the advantages of the proposed high-fidelity model over simplified counterpart. A clearer comparison between the experimental and modelled results can be obtained

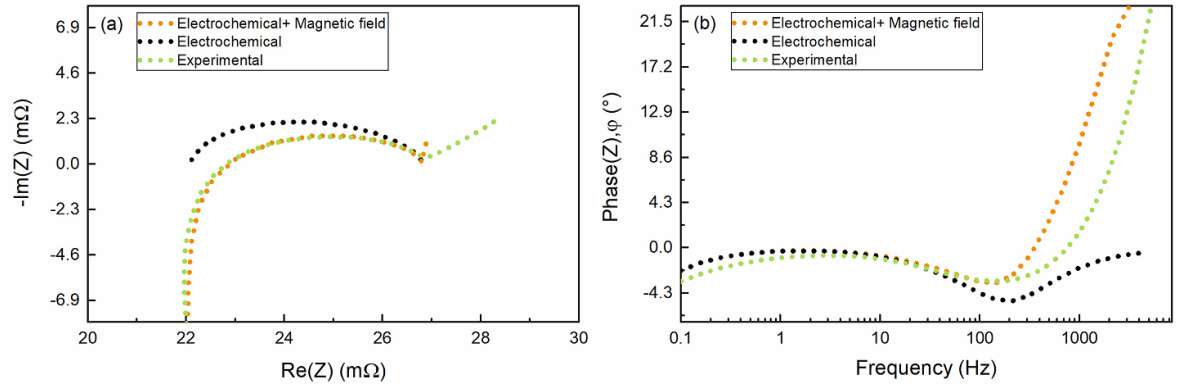

Figure 4. Comparisons between model predictions and experimental results shown in the Nyquist plot (a) and phase angle plot (b).

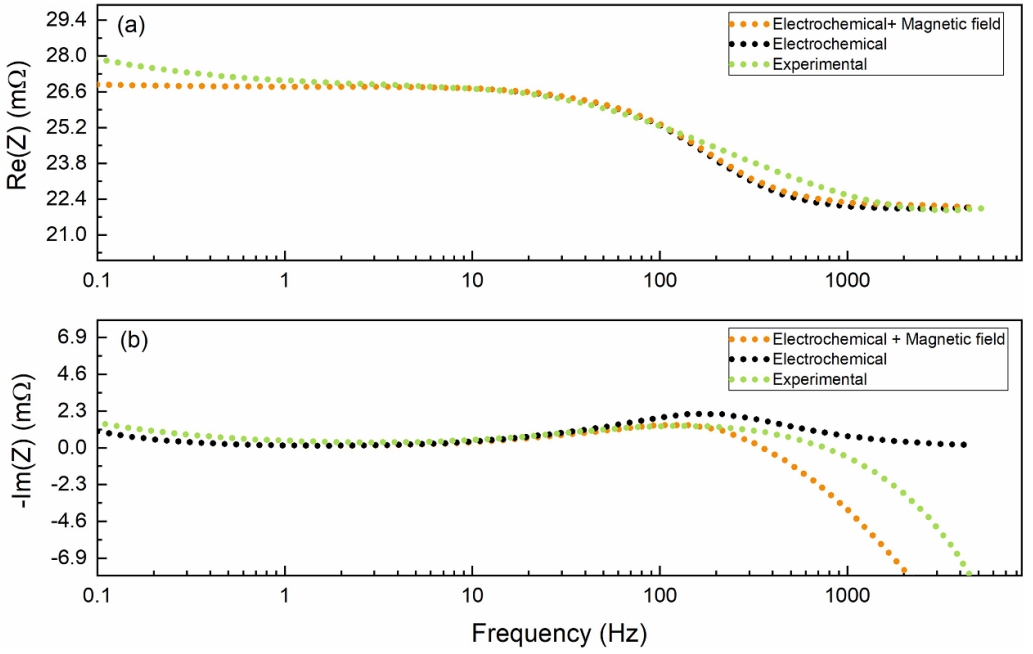

Figure 5. Real (a) and imaginary (b) parts of impedance versus frequency, showing results from the electrochemical model (black), the model with electromagnetic integration (orange), and the in-house experimental data (green).

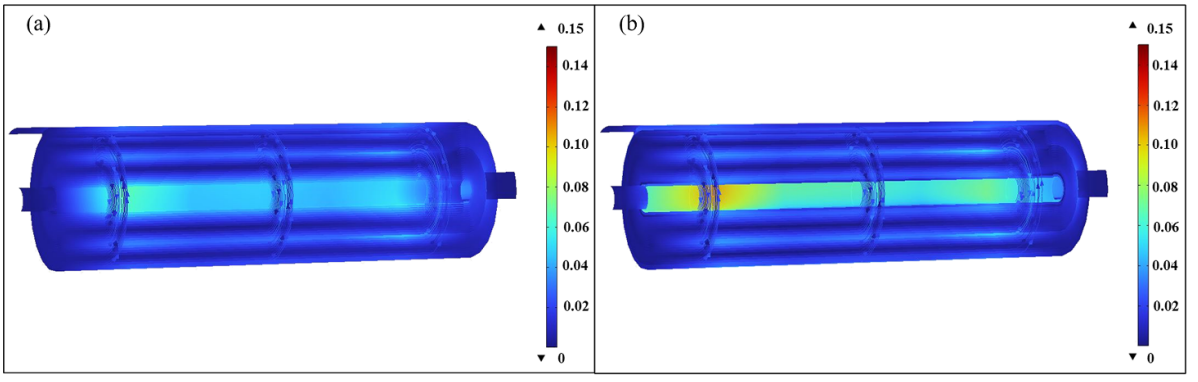

Figure 6. Magnetic field **B** in mT at 0.1 kHz (a) and 5 kHz (b), with corresponding current vectors shown as arrows on 3 different z-planes.

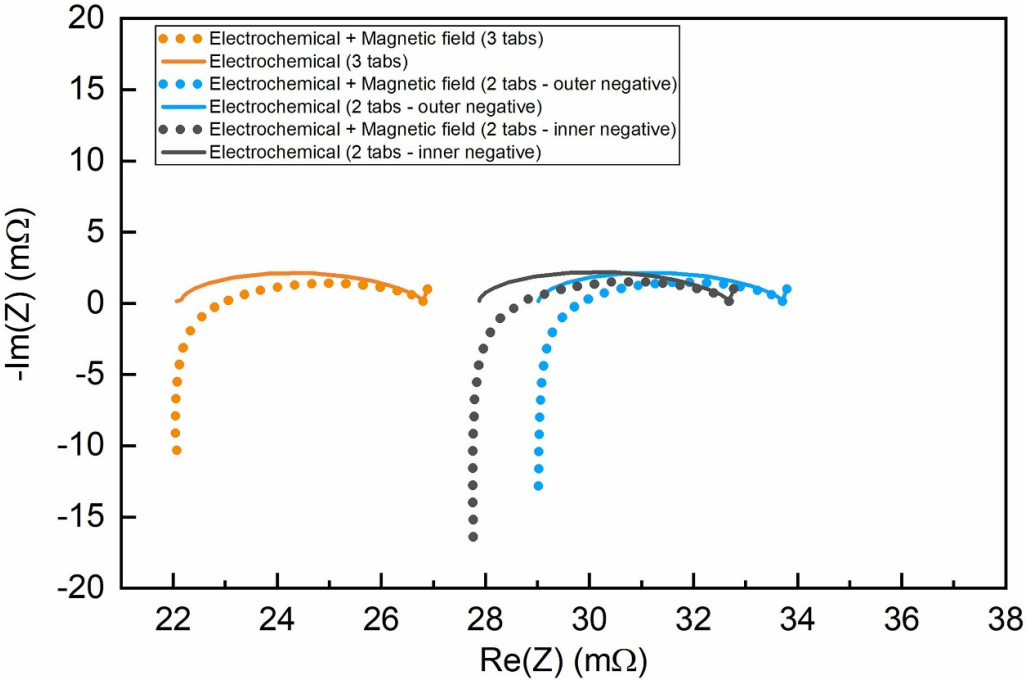

Figure 7. Nyquist diagram of impedance for different tab configurations.

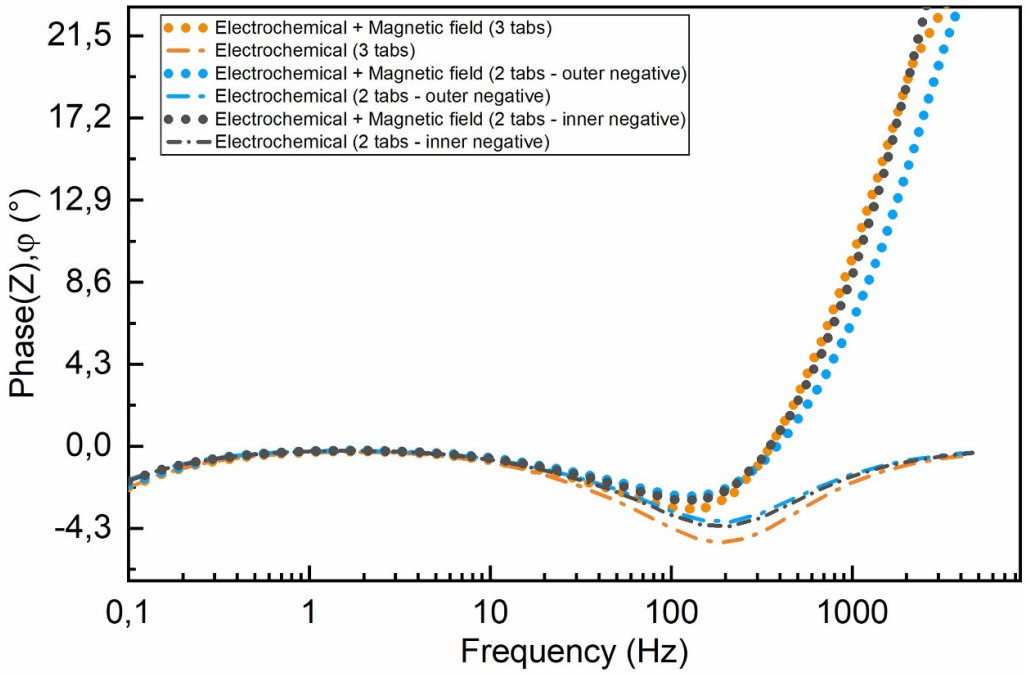

Figure 8. Phase angle plot of cells with different tab configurations.

by examining the impedance as a function of frequency using Bode plots, as shown in Figs. 5a and 5b. In addition, the inductive effect can be observed from about 100 Hz, which is consistent with the earlier work of Coman et al.[5] The detailed 3D representation of the jellyroll captures the different properties of the individual material layers and provides a more realistic representation of the current paths, that are based on the coiled structure. As a result, the P4D model represents an advance over the P2D model as it is able to capture the inherent resistance of the current collector, an element missing from the P2D model.[6] Figure 6 shows the magnetic field together with the corresponding current vectors, which are represented as arrows in three different Z planes within the cell.

When inductive effects are included, the P4D model shows closer agreement with experimental impedance measurements at high frequencies. This extends the work of Coman et al.,[5] whose model provided the foundation for the present study, by incorporating a detailed 3D geometry and by explicitly accounting for electromagnetic effects in the jellyroll structure.

When either the inner or outer negative tab is removed from the original cell configuration, while keeping all other parameters

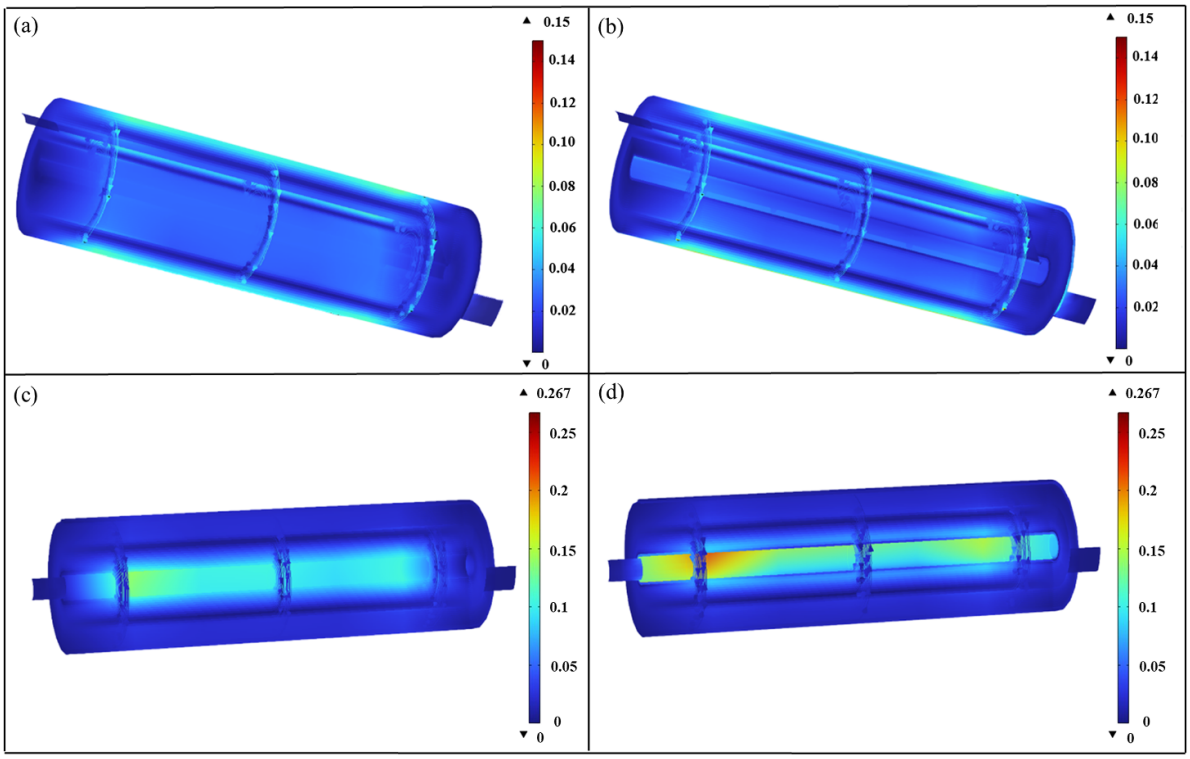

Figure 9. Magnetic field B (mT) at 0.1 kHz for the inner negative tab (a) and outer negative tab (c), and at 5 kHz for the inner negative tab (b) and outer negative tab (d), with corresponding current vectors shown as arrows on three different z-planes.

and the jellyroll geometry unchanged, it becomes clear that even small geometric modifications can significantly affect the impedance response and inductive behavior. If only a negative tab is present, as shown in Fig. 7, there is a significant shift in the real part of the impedance toward a higher resistance. This shift is related to the change in the current paths within the cell, which affects both the electrochemical and electromagnetic behavior.

At higher frequencies, a more pronounced inductive response is visible both in the Nyquist diagram (Fig. 7) and in the phase angle plots (Fig. 8). The magnetic field characteristics shown in Fig. 9 at frequencies of 0.1 kHz–5 kHz show that the magnetic field distribution is more uniform over both frequencies when only the outer negative tab is used. This uniformity is due to a wider and more uniform current flow throughout the cell.

On the other hand, configurations with only the inner negative tab result in stronger, more localized magnetic fields. These amplified fields lead to a noticeable increase in inductive responses, as confirmed by the impedance data. The phase angle diagrams further emphasise this. They show more pronounced phase shifts and indicate stronger inductive effects for the configuration with the inner negative tab compared to the outer-tab configuration.

Conclusions

We have proposed and validated a generic modelling framework for the fully coupled modelling of electrochemical-electromagnetic phenomena in 3D by coupling electrochemical and transport phenomena with Maxwell–Ampère's law to allow a comprehensive analysis of impedance with particular emphasis on the high-frequency range. The features and capabilities of the model are demonstrated using the cylindrical 21 700 Li-ion cell, which represents a realistic yet descriptive geometry to demonstrate the importance of a consistent 3D geometric description of the cell. In contrast to conventional P2D models with simplified geometric representation of electromagnetic phenomena, this approach captures the complex interactions between electrochemical processes and electromagnetic phenomena, resulting in a more accurate representation of battery impedance. The most significant improvement of this model is the ability to explicitly account for the influence of the jellyroll configuration on high-frequency inductive responses by simulating the magnetic field generated by the current flow in the electrochemical model through a realistic jellyroll representation. The results highlight the capability of the 3D model to accurately characterize the impedance features observed in Nyquist and Bode plots, including the inductive behavior at high frequencies attributed to the jellyroll geometry. Factory quality control and end-of-line testing can directly use these insights to analyze rapid, high-frequency impedance fingerprints. This approach enables the non-destructive screening of internal manufacturing flaws, such as faulty tab welding, layer misalignments, or structural defects. This model enables a deeper understanding of how design features such as cell geometry influence the overall impedance response. Although the model successfully captures the key phenomena, further research could explore more complex geometries and incorporate additional battery components, such as current interrupting devices, which could influence inductive behavior. Nonetheless, this fully 3D-based approach provides a robust tool to improve battery design, improving EIS analysis and model-based deciphering of EIS spectra, and promote the development of more efficient, durable and reliable energy storage solutions.

Acknowledgements

The authors acknowledge support from the European Union's Horizon 2020 research and innovation programme under Grant Agreement No. 101069743 (ADVAGEN). The authors also acknowledge financial support from the Slovenian Research Agency (research core Funding No. P2-0401).

ORCID

Piera Di Prima https://orcid.org/0009-0007-9063-6537
Igor Mele https://orcid.org/0000-0002-9071-7325
Silvia Bodoardo https://orcid.org/0000-0002-3579-9778
Massimo Santarelli https://orcid.org/0000-0001-6778-3546
Tomaž Katrašnik https://orcid.org/0000-0001-6954-4936
Julia Amici https://orcid.org/0000-0003-4369-317X

References

1. N. Meddings, M. Heinrich, F. Overney, J.-S. Lee, V. Ruiz and E. Napolitano, "Application of electrochemical impedance spectroscopy to commercial Li-ion cells: a review." *J. Power Sources*, **480**, 228742 (2020).
2. F. Ciucci, "Modeling electrochemical impedance spectroscopy." *Curr. Opin. Electrochem.*, **13**, 132 (2019).
3. S. T. Bakenhaster and H. D. Dewald, "Electrochemical impedance spectroscopy and battery systems: past work, current research, and future opportunities." *J. Appl. Electrochem.*, **55**, 1657 (2025).
4. T. F. Landinger, G. Schwarzberger and A. Jossen, "A novel method for high frequency battery impedance measurements," in *2019 IEEE Int. Symp. on Electromagnetic Compatibility, Signal and Power Integrity (EMC + SIPI)*, (2019).
5. P. T. Coman, R. Mollah, N. Irish, S. Karuppuswami, S. T. Dix and W. Johnson, "Electrochemical-electromagnetic coupled physics-based mathematical modeling of li-ion batteries: a theoretical proof of concept." *J. Electrochem. Soc.*, **170**, 120528 (2023).
6. F. C. Laman, M. W. Matsen and J. A. R. Stiles, "Inductive impedance of a spirally wound Li/MoS_2 cell." *J. Electrochem. Soc.*, **133**, 2441 (1986).
7. X. Du, J. Meng, Y. Amirat, F. Gao and M. Benbouzid, "Exploring impedance spectrum for lithium-ion batteries diagnosis and prognosis: a comprehensive review." *J. Energy Chem.*, **95**, 464 (2024).
8. A. C. Lazanas and M. I. Prodromidis, "Electrochemical Impedance Spectroscopy—A Tutorial." *ACS Meas. Sci. Au.*, **3**, 162 (2023).
9. S. D. Talian, S. Brutti, M. A. Navarra, J. Moškon and M. Gaberšček, "Impedance spectroscopy applied to lithium battery materials: good practices in measurements and analyzes." *Energy Storage Mater.*, **69**, 103413 (2024).
10. L. M. Knott, E. Long, C. P. Garner, A. Fly, B. Reid and A. Atkins, "Insights into lithium-ion battery cell temperature and state of charge using dynamic electrochemical impedance spectroscopy." *Int. J. Energy Res.*, **2024**, 9657360 (2024).
11. J. P. Meyers, M. Doyle, R. M. Darling and J. Newman, "The impedance response of a porous electrode composed of intercalation particles." *J. Electrochem. Soc.*, **147**, 2930 (2000).
12. I. J. Ong and J. Newman, "Double-layer capacitance in a dual lithium ion insertion cell." *J. Electrochem. Soc.*, **146**, 4360 (1999).
13. G. Sikha and R. E. White, "Analytical Expression for the Impedance Response of an Insertion Electrode Cell." *J. Electrochem. Soc.*, **154**, A43 (2007).
14. M. Doyle and J. Newman, "Modeling the performance of rechargeable lithium-based cells: design correlations for limiting cases." *J. Power Sources*, **54**, 46 (1995).
15. M. Doyle, T. F. Fuller and J. Newman, "Modeling of galvanostatic charge and discharge of the lithium/polymer/insertion cell." *J. Electrochem. Soc.*, **140**, 1526 (1993).
16. T. F. Fuller, M. Doyle and J. Newman, "Simulation and optimization of the dual lithium ion insertion cell." *J. Electrochem. Soc.*, **141**, 1 (1994).
17. M. Doyle, J. P. Meyers and J. Newman, "Computer simulations of the impedance response of lithium rechargeable batteries." *J. Electrochem. Soc.*, **147**, 99 (2000).
18. B. Wimarshana, I. Bin-mat-arishad and A. Fly, "A multi-step parameter identification of a physico-chemical lithium-ion battery model with electrochemical impedance data." *J. Power Sources*, **580**, 233400 (2023).
19. X. Kong, G. L. Plett, M. S. Trimboli, Z. Zhang, D. Qiao and T. Zhao, "Pseudo-two-dimensional model and impedance diagnosis of micro internal short circuit in lithium-ion cells." *J. Energy Storage*, **27**, 101085 (2020).
20. V. Laue, F. Röder and U. Krewer, "Practical identifiability of electrochemical P2D models for lithium-ion batteries." *J. Appl. Electrochem.*, **51**, 1253 (2021).
21. Y. Xie, J. Li and C. Yuan, "Mathematical modeling of the electrochemical impedance spectroscopy in lithium ion battery cycling." *Electrochim. Acta*, **127**, 266 (2014).
22. I. Mele, K. Zelič, M. Firm, J. Moškon, M. Gaberšček and T. Katrašnik, "Enhanced porous electrode theory based electrochemical model for higher fidelity modelling and deciphering of the EIS spectra." *J. Electrochem. Soc.*, **171**, 080537 (2024).
23. X. Wang, X. Wei, J. Zhu, H. Dai, Y. Zheng, X. Xu and Q. Chen, "A review of modeling, acquisition, and application of lithium-ion battery impedance for onboard battery management." *eTransportation*, **7**, 100093 (2021).
24. N. Hallemans, "Electrochemical impedance spectroscopy beyond linearity and stationarity—a critical review." *Electrochim. Acta*, **466**, 142939 (2023).
25. J. Estaller, A. Kersten, M. Kuder, T. Thiringer, R. Eckerle and T. Weyh, "Overview of battery impedance modeling including detailed state-of-the-art cylindrical 18650 lithium-ion battery cell comparisons." *Energies*, **15**, 3822 (2022).
26. A. Kersten, J. Estaller, M. Kuder, T. Thiringer and T. Weyh, "Online estimation of the high-frequency intercept resistance for electrochemical impedance spectroscopy in electric vehicles." *IEEE Trans. Power Electron.*, **36**, 13390 (2021).
27. T. L. Kirk, "Nonlinear electrochemical impedance spectroscopy for lithium-ion battery model parameterization." *J. Electrochem. Soc.*, **170**, 010514 (2023).
28. M. Fleckenstein, O. Bohlen, M. A. Roscher and B. Bäker, "Current density and state of charge inhomogeneities in Li-ion battery cells with $LiFePO_4$ as cathode material due to temperature gradients." *J. Power Sources*, **196**, 4769 (2011).
29. M. Xu, Z. Zhang, X. Wang, L. Jia and L. Yang, "Two-dimensional electrochemical–thermal coupled modeling of cylindrical $LiFePO_4$ batteries." *J. Power Sources*, **256**, 233 (2014).
30. W. B. Gu and C. Y. Wang, "Thermal-electrochemical modeling of battery systems." *J. Electrochem. Soc.*, **147**, 2910 (2000).
31. S. Baazouzi, N. Feistel, J. Wanner, I. Landwehr, A. Fill and K. P. Birke, "Design, properties, and manufacturing of cylindrical Li-Ion battery cells—a generic overview." *Batteries*, **9**, 309 (2023).
32. M. N. Akram, K. Xu and G. Chen, "Structure simplification of planar quadrilateral meshes." *Comput. Graph.*, **109**, 1 (2022).
33. P. Di Prima, D. Dessantis, D. Versaci, J. Amici, S. Bodoardo and M. Santarelli, "Understanding calendar aging degradation in cylindrical lithium-ion cell: a novel pseudo-4-dimensional electrochemical-thermal model." *Appl. Energy*, **377**, 124640 (2025).
34. C.-H. Chen, F. B. Planella, K. O'regan, D. Gastol, W. D. Widanage and E. Kendrick, "Development of experimental techniques for parameterization of multi-scale lithium-ion battery models." *J. Electrochem. Soc.*, **167**, 080534 (2020).
35. A. Merzouki and N. Haddaoui, "Electrical conductivity modeling of polypropylene composites filled with carbon black and acetylene black." *ISRN Mater. Sci.*, **2012**, 493065 (2012).
36. M. T. von Srbik, M. Marinescu, R. F. Martinez-botas and G. J. Offer, "A physically meaningful equivalent circuit network model of a lithium-ion battery accounting for local electrochemical and thermal behavior, variable double layer capacitance and degradation." *J. Power Sources*, **325**, 171 (2016).
37. M. V. Morganti, S. Longo, M. Tirovic, C. Y. Blaise and G. Forostovsky, "Multi-scale, electro-thermal model of NMC battery cell." *IEEE Trans. Veh. Technol.*, **68**, 10594 (2019).
38. E. W. C. Spotte-smith, S. M. Blau, X. Xie, H. D. Patel, M. Wen and B. Wood, "Quantum chemical calculations of lithium-ion battery electrolyte and interphase species." *Sci. Data*, **8**, 203 (2021).
39. E. Peled and S. Menkin, "Review—SEI: past, Present and Future." *J. Electrochem. Soc.*, **164**, A1703–A19 (2017).
40. R. C. McNulty, E. Hampson, L. N. Cutler, C. P. Grey, W. M. Dose and L. R. Johnson, "Understanding the limits of Li-NMC811 half-cells." *J. Mater. Chem. A*, **11**, 18302 (2023).